Applied Catalysis B: Environmental 248 (2019) 526–537

Contents lists available at ScienceDirect

Applied Catalysis B: Environmental

journal homepage: www.elsevier.com/locate/apcatb

Catalytic performance and an insight into the mechanism of CeO_2 nanocrystals with different exposed facets in catalytic ozonation of p-nitrophenol

Shahzad Afzal, Xie Quan*, Sen Lu

Key Laboratory of Industrial Ecology and Environmental Engineering (Ministry of Education), School of Environmental Science and Technology, Dalian University of Technology, Linggong Road 2#, Dalian, 116024, PR China

ARTICLE INFO

Keywords:
Catalytic ozonation
CeO_2
Ceria exposed facets
Oxygen vacancies
Defect sites

ABSTRACT

Ceria based catalysts have been widely applied in ozonation of organic pollutants in wastewater treatment. Ceria with different exposed facets have not been used in catalytic ozonation. In this study, ceria nanorods (R-CeO_2), nanocubes (C-CeO_2) and nanooctahedra (O-CeO_2) with different exposed facets (110) + (100), (100) and (111)) respectively were used in catalytic ozonation of p-nitrophenol. Two calcination temperatures 300 and 500 °C were selected for comparative catalytic activity. Ceria nanoparticles (NP-CeO_2) were also prepared for comparative catalytic activity. Approximately 86%, 71%, 68%, 64%, 60% and 40% TOC was removed by ozonation catalyzed by R300-CeO_2, C300-CeO_2, CeO_2-NP, O300-CeO_2, R500-CeO_2 and ozonation alone respectively. Nanorod calcined at 500 °C (R500-CeO_2) showed lower catalytic activity as compared to R300-CeO_2. O_3 was also rapidly decomposed by R300-CeO_2 as compared to other catalysts and single ozonation. Inorganic hydroxyl radical scavengers and several characterization techniques were applied for investigating the underlying mechanism of catalytic ozonation. Hydroxyl radicals, surface peroxide and surface atomic oxygen as reactive oxygen species were generated for enhancing the catalytic activity. Furthermore, irrespective of surface area, the difference in catalytic activity of ceria nanoshapes were assigned to the differences in the abundance of surface basic sites, defects densities/oxygen vacancies (OVs) and coordination number of surface atoms. This study provides an insight to use other metals with variety of exposed facets for catalytic ozonation.

1. Introduction

Heterogeneous catalytic ozonation has been extensively used for enhancing the abatement of refractory organic pollutants in water treatment [1,2]. Various organic pollutants such as phenolics [3,4], pesticides [5,6], nitrobenzenes [7–9] dyes [10,11], pharmaceuticals [12–14], phthalic acid esters [15,16] and some others [17,18] have been used in catalytic ozonation. Until now, different metals, metal oxides and /or metal oxides supported on various solids (silica, carbons, alumina and some others), minerals and carbon materials etc have been used as heterogeneous ozonation catalysts. As a matter of fact, carbon materials as ozonation catalysts possess high adsorption capability but unfortunately can be oxidized in the process of ozonation. Furthermore, metals or metal oxides loaded on various supports usually undergo steric hindrance, causing distorted textural properties (pore size, pore volume and surface area), pore blockage, poor accessibility of active sites to reactants and an uneven active components distribution. Moreover, due to complexity in the synthesis of metal oxides/metals incorporated porous materials/catalyst supports, exploring the mechanism of catalytic ozonation is still unclear [19,20]. Despite enormous research in catalytic ozonation, there is still a quest for finding/synthesizing an efficient and stable catalyst, and ultimately understanding/proposing the mechanism of catalytic ozonation.

Ceria (CeO_2) has been extensively applied in many research areas such as CO preferential oxidation, soot combustion, fuel cells, oxygen sensors, and transformation of a variety of organic molecules due to its abundant oxygen vacancies (OVs), versatile acid-base properties, low redox potential and relative abundance [21–24]. Due to the aforementioned electrochemical properties, ceria as a heterogeneous catalyst has been widely applied in catalytic ozonation in waste water treatment as a standalone (single metal) catalyst, composite with other metals, as a support for other metals/metal oxides and ceria loaded on support [25–28]. In spite of promising results, these studies mostly concentrated on the enhanced catalytic activity by merely investigating the

* Corresponding author.
E-mail address: quanxie@dlut.edu.cn (X. Quan).

https://doi.org/10.1016/j.apcatb.2019.02.010
Received 19 August 2018; Received in revised form 7 January 2019; Accepted 7 February 2019
Available online 16 February 2019
0926-3373/ © 2019 Elsevier B.V. All rights reserved.

comparative catalytic activity of single component ceria or in composite with other transition metals, increasing the surface area by loading it on specific supports and the role of redox couple (Ce^{3+}/Ce^{4+}), while the investigation of some key surface factors such as abundance of OVs, surface basicity and surface hydroxyl groups coverage as a function of different exposed crystal facets with different coordinative unsaturated sites is still not reported.

Recently, ceria with different nanoshapes such as nanorods, nanooctahedra and nanocubes with (110) + (100), (111) and (100) crystal facets respectively have been attracting enormous attention in multi-purpose applications [29–31]. For example, extensive research [21,32,33] have been conducted to investigate CO oxidation on CeO_2 facet-dependent catalysts. These studies depicted the facet-dependent interaction of CO with CeO_2 and found that the ceria dominated with (110) and (100) facets were more active in catalytic activities than with (111) facets. Theoretical investigation showed that the energy of oxygen vacancy formation, the nature and concentration of defect sites significantly influenced the catalytic efficiency of ceria with different crystal facets. Thermodynamically, CeO_2 (111) facets are the most stable facet [34]. Usually ceria wires or rod-like shapes expose (110) + (100) facets in combination [32,33,35]. However, recently it is suggested that, due to different calcination temperature, ceria nanorods and nanowires expose various facets, including (111) facets with abundant structural defects [36]. Ceria has strong basicity but weaker acidity [37]. The surface geometry influences the coordination numbers and positions of acidic and basic sites which alter the catalytic activity. Generally the calculated oxygen-vacancy formation energies obey the order of (111) > (100) > (110) [38] which can influence the adsorption behavior of surface adsorbates and redox property [39]. Hydroxyls groups are important to create and propagate clusters of oxygen vacancies (OVs) while the adjoining OH groups play an important role in stabilizing the thermodynamically unstable OVs clusters [40].

Considering the significance of the exposed crystal facets in interfacial reactions, ozone and organic intermediates may show different behavior on these surfaces which can lead to different catalytic activity. Previous studies regarding the use of ceria for catalytic ozonation mainly dealt with increasing the surface area and the role of redox couple. The detailed mechanistic study of using ceria nanoshapes such as nanorods, nanooctahedra and nanocubes with (110) + (100), (111) and (100) exposed crystal facets in catalytic ozonation is still not reported. In catalytic ozonation, the previous investigations have proposed contradictory mechanisms and still there is no unified mechanism. Our study is aimed to use CeO_2 nanoshapes with different exposed crystal facets for getting a mechanistic insight into understanding the effect of the surface properties in terms of OVs abundance, the relative abundance of Ce^{3+}/Ce^{4+}, surface basicity and surface OH group's coverage in enhancing the catalytic performance. Herein, p-nitrophenol (PNP), one of the top priority organic pollutants is selected for mineralization in ozonation catalyzed by ceria nanoshapes.

2. Experimental section

2.1. Chemicals and reagents

All NaOH, KI, KNO_3, Na_2HPO_4 and $Na_2S_2O_3$ were supplied by Tianjin Damao Chemical Co., Ltd. HCl was supplied by Tianjin Fuyu Fine chemicals Co., Ltd. Ultrapure water (18.2 MΩ cm) was used during all the experiments. $Ce(NO_3)_3.6H_2O$, $NaHCO_3$, Na_2SO_4, $NaHSO_3$, NH_4OH, urea, HNO_3, Terephthalic acid, DMPO (5,5-dimethyl-1-pyrroline), TEMP (2,2,6,6-tetramethyl-4-piperidone) and p-nitrophenol were purchased from Aladdin Industrial Corporation. All the chemicals and reagents were used without further purification.

2.2. Synthesis of ceria catalysts

Ceria nanoshapes were synthesized according to ref [35]. Typically, 0.868 g $Ce(NO_3)_3{\cdot}6H_2O$ as ceria precursor was dissolved in 5 mL deionized water to make solution A. Then 0.01 M NaOH (0.016 gm) for octahedral shape while 6.0 M NaOH (9.60 gm) for rod and cubic shape were dissolved in 35 mL water in separates beakers to make solution B. Then solution A was put drop-wise into the solution B with continuous stirring at room temperature. This mixture was further stirred for 30 min, and then hydrothermally treated in 100 mL Teflon-lined autoclaves for 24 h at 100 °C for rod shaped morphology and 180 °C for both cubic and octahedral morphology. Then it was cooled down to room temperature, centrifuged to collect white precipitates and washed several times with deionized water. As the previous reports [41] have proved that the presence of residual Na^+ can affect the acid-base properties and reactivity of ceria, so it was eliminated by rinsing it in 2 mL of 0.1 M NH_4OH under sonication for 5 min. The product was centrifuged and washed many times with deionized water. For further neutralization, it was treated with 2 mL of 0.1 M HNO_3 under sonication for 5 min. Then it was washed multiple times with ultra-pure water and ethanol until the neutral pH. The product was vacuum dried at 100 °C for 8 h. All these catalysts were calcined at 300 °C in air for 4 h. Ceria nanorod, nanocube and nano-octahedra were represented as R300-CeO_2, C300-CeO_2 and O300-CeO_2 respectively. One of the selected catalysts (nanorod) was also calcined in air at 500 °C for 4 h to investigate its catalytic activity at high calcination temperature. This was labeled as R500-CeO_2. Similarly, ceria nanoparticles without any exact morphology/facets were prepared by urea-hydrothermal process [42]. For this, $Ce(NO_3)_3.6H_2O$ as cerium precursor and urea (1:3 molar ratio) were dissolved in deionized water, followed by heating at 140 °C for 5 h in 100 mL autoclave. The white product was centrifuged and washed with deionized water and ethanol multiple times until neutral pH. The product was dried at 120 °C for 2 h and calcined at 450 °C for 4 h. The CeO_2 nanoparticles were labelled as NP-CeO_2.

2.3. Characterization methods

XRD analyses were carried out by PANalytical B.V. Empyrean on a Rigaku DMAX III VC X-ray diffractmeter using Cu Kα radiation at 0.1542 nm. The N_2 sorption isotherms were recorded on a Quantasorb surface area analyzer (QuadraSorb station 1, Quantachrome Corp., USA). The specific surface area was obtained by BET method while other pore dimensions by the BJH method. The morphology of nanocatalysts were obtained by the transmission electron microscopy (TEM, TecnaiG2 20, FEI, USA). The leached Ce during catalytic ozonation was quantified by ICP-AES (Optima 200 DV). The X-rays photoelectronspectroscopy (XPS) analyses were carried out on AVGESCALAB 250 spectrometer equipped with a non monochromatized AlKX-ray source operated at eV = 1.602×10^{-19} J and 1 bar = 100 kPa (1486.6 eV). The linear sweep voltammetry (LSV) measurements were carried in the presence of 0.1 M Na_2SO_4 with and without ozone. The pH_{pzc} of the selected nanorods was measured by Malvern Zetasizer Nano ZS. Surface hydroxyl (OH) groups on the catalysts were quantified by thermogravimetric analysis (TGA) on TG/DT A6300, SII Nanotechnology lnc analyzer at 700 °C @ 10 °C min^{-1} under N_2 flow in two phases: (1) at a range of 30–120 °C and kept it at 120 °C for 15 min in isothermal condition (2) subsequently followed by 120–700 °C. F-4500; Hitachi Fluorescence spectrophotometer was used to measure fluorescence spectra of 2-hydroxyterephthalic at an excitation wavelength of 315 nm. Raman measurements were carried out on DXR Smart Raman (Thermo fisher) with and without ozone. For this, 100 mg R300-CeO_2 was suspended in 3 mL ultra-pure water and gaseous O_3 was injected into it for 15 min. 0.5 mL suspension was put on the reaction cell and scanned in the range of 400-1200 cm^{-1}. The EPR (electron paramagnetic resonance) analyses were conducted on a Bruker EPR I200 spectrometer to determine reactive intermediates species generated during catalytic ozonation. R300-CeO_2 and O_3 stock solution were mixed well with 100 mM DMPO in deionized water. Then immediately a specific volume was injected into a capillary tube, and then at room temperature, the

spectra were recorded according to these conditions: EPR Spectra by using DMPO: sweep width = 100.0 G, modulation frequency = 100 GHz, microwave frequency = 9.42 GHz, microwave power = 16.73 mW and Centerfield = 3360.0 G. EPR Spectra using TEMP: microwave power: 4.25 mW, sweep width = 100 G, centerfield = 3510 G, modulation frequency = 100 GHz, microwave frequency = 9.42 GHz. TPD-CO_2 analyses were carried out on a ChemBET Pulsar TPR/TPD mounted with Automated Chemisorptions Analyzer (Quantachrome Corporation, USA). For TPD-CO_2, 0.10 g catalyst was preheated under He stream at 350 °C, then cooled down to 50 °C, ultimately subjected to a mixture of 10% CO_2 in He @ 30 mL/min. The excess CO_2 was flushed out by passing He through it. Ultimately, the temperature was increased to 900 °C @ 10 °C/min under He flow and desorption data was taken. Similarly, temperature programmed desorption of oxygen (TPD-O_2) analysis was performed on the aforementioned instrument used for TPD-CO_2. For this, 100 mg ceria solid was preheated at 350 °C under He flow (30 mL/min), followed by cooling to 50 °C. Then O_2 gas was flowed (30 mL min^{-1}) at room temperature through the preheated sample. The excess O_2 was removed by purging He through the sample. Subsequently, it was heated to 900 °C with 10 °C/min ramp in He stream (30 mL min^{-1}), followed by the detection of O_2 desorption. Similarly Temperature programmed reduction of H_2 (TPR- H_2) was performed on the same instrument as used for TPD-CO_2 and TPD-O_2. Approximately 50 mg solid catalyst was pretreated at 500 °C for an hour in 30 mL min^{-1} N_2 gas, then cooled to room temperature. TPR analysis was carried out in 10% H_2/Ar mixture having flow rate of 10 mL min^{-1} with heating from room temperature to 900 °C at 5 °C min^{-1} ramp.

2.4. Catalytic ozonation and analytical procedures

Catalytic ozonation and ozonation were carried out in 300 mL cylindrical shaped glass reactor in semi-batch mode. 250 mL of 25 mg L^{-1} p-nitrophenol solution (PNP) and 0.10 g catalysts (if used) were added under continuous stirring speed of 1600 rpm (optimized speed) at room temperature. The pH of solution was kept at the real pH (5.75) of PNP solution. The schematic representation of semi batch system and other devises is given in supporting information in Fig S1. O_3 gas was generated by ozone generator (made in Germany) with continuously injecting O_2 in dry pure form with flow rate of 0.2 L min^{-1}. The ozone was fed continuously into the PNP solution at the bottom of the reactor. At specific time interval, an appropriate amount of sample was taken for TOC analysis, followed by an immediate filtration to remove suspended particles. Remaining aqueous O_3 in the samples was quenched by an appropriate amount of 0.1 M $Na_2S_2O_3$ solution. The adsorption capability of the catalysts was evaluated by the same aforementioned procedure in the presence of oxygen stream (without ozone). Solution pH was measured by METTLER TOLEDO pH meter. Aqueous O_3 concentration was monitored by an instrument called Dissolved Ozone System (ATI MODEL Q45, USA) while O_3 in gas phase was measured by iodometric method [43]. TOC analysis was carried out by TOC analyzer (multi N/C®2100 TOC analysis meter, ANALYTIKJENA, GER). All the experiments were conducted in triplicates. Catalytic ozonation in the presence of R300-CeO_2 was carried with different stirring speeds such as 1600 rpm, 1800 rpm and 2000 rpm (Fig S2, Supporting information) and there was no significant change in the efficiency of catalytic ozonation. The catalytic ozonation followed the kinetic regime as the catalytic efficiency was not affected by stirring speed. So stirring speed of 1600 rpm was selected for catalytic ozonation of PNP and ozone decomposition. Ozone decomposition experiments were carried out in a sealed batched type glass reactor. At first, gaseous ozone was continuously diffused into 0.5 L deionized water without PNP and catalysts until 10 mg L^{-1} of aqueous ozone concentration was obtained. Then for catalytic ozonation, catalyst was immediately added into the reactor, magnetically stirred for mixing well and favorable mass transfer. Prior to analyzing of ozone, the catalyst was separated from the suspension by filtration to avoid the adsorption of O_3 on the catalyst. Before filtration, the filter was rinsed with O_3 stock solution. O_3 concentration was monitored at specific intervals of time.

3. Results and discussion

3.1. Characterization of ceria

The TEM images (Fig. 1) of CeO_2 nanoshapes depicted the typical morphologies of nanorods, nanocubes and nano-octahedra. HRTEM of

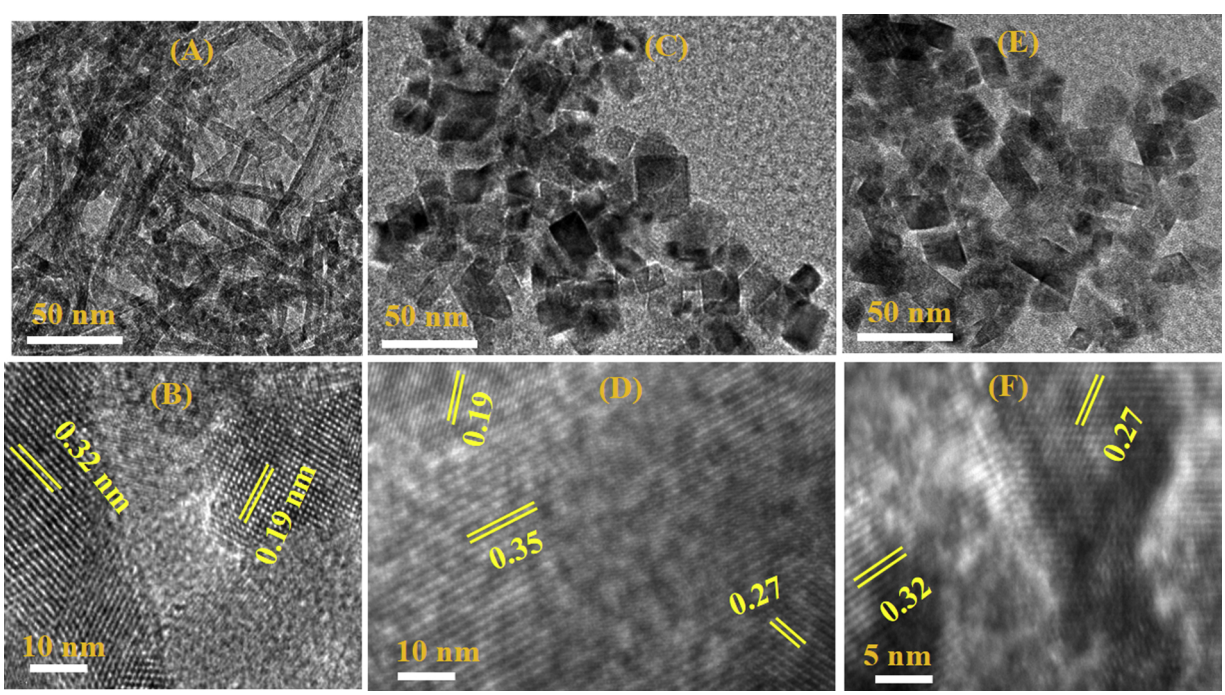

Fig. 1. (A, B) TEM and HRTEM micrographs of R300-CeO_2, (C, D) C300-CeO_2 and (E, F) O300-CeO_2.

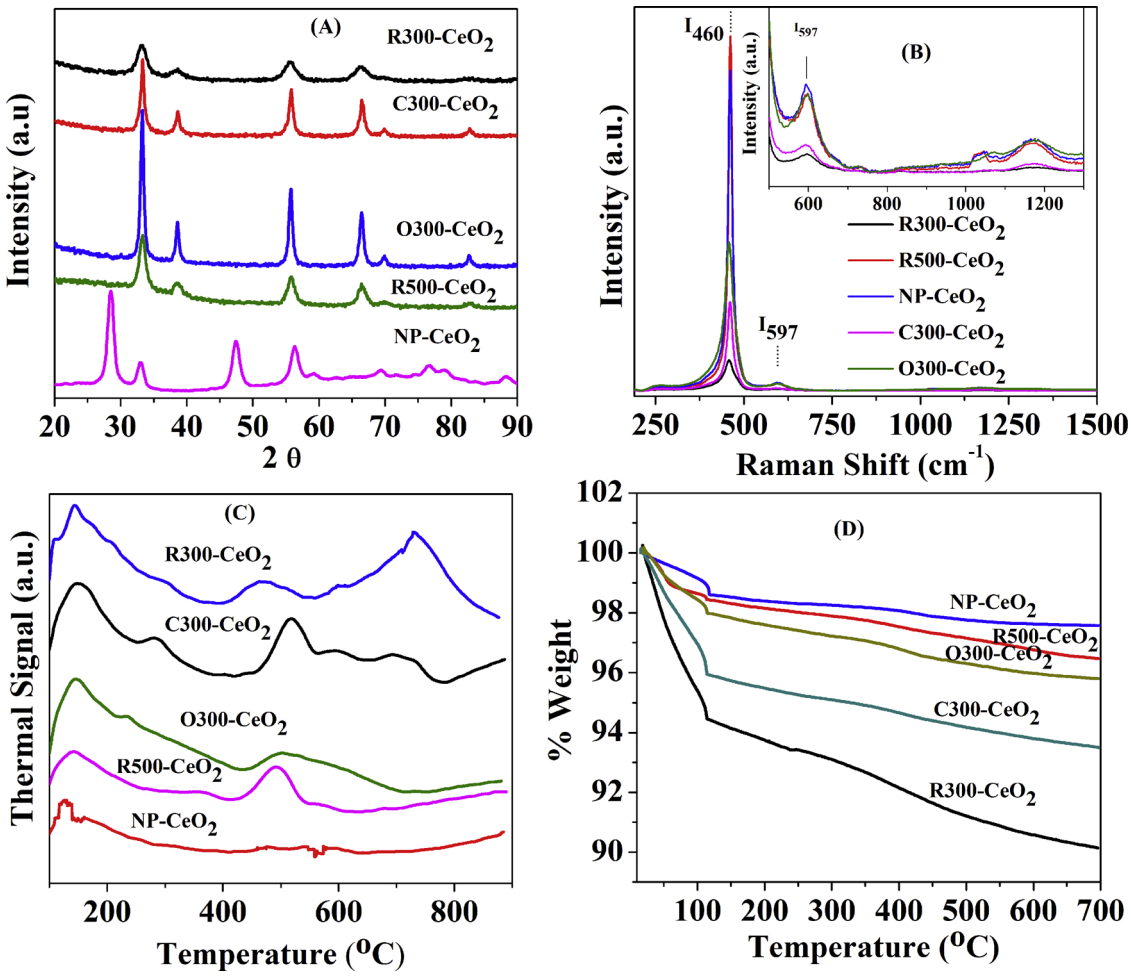

Fig. 2. (A) XRD analyses of all catalyst, (B) Raman Spectroscopy of CeO_2 nanoshapes and nanoparticles. The inset in Fig B indicates its magnified spectra at I_{597}, (C) TPD-CO_2 of all CeO_2 nanoshapes and nanoparticles, (D) TGA measurements of all catalysts.

R300-CeO_2 (Fig. 1B) depicted the lattice planes with 0.32 and 0.19 nm spacing, attributed to (111) and (220) planes respectively. R300-CeO_2 depicted a 1D growth with a preferred direction along the [110] facet, which is enclosed by (220) planes. HRTEM image (Fig. 1D) of nanocubes showed (111), (200) and (220) lattice planes with spacing of 0.35, 0.27 and 0.19 nm respectively. The HRTEM image of nanooctahedra in Fig. 1F showed (111) and (200) lattice planes with spacing of 0.32 and 0.27 nm respectively [35,44].

As shown in Fig. 2A, XRD peaks of the three ceria polymorphs could be indexed to the typical XRD patterns of pure fluorite cubic structures of CeO_2 (Fm3m (225), ICDD 00-001-0800).The XRD patterns of nanocubes and nano-octahedra showed relatively higher intensity than the nanorods. NP-CeO_2 depicted the typical XRD peaks of fluorite structure of CeO_2 (JCPDS 34-0349). Moreover, the XRD peaks for nanorods became more intense after calcination at 500 °C.

As the redox catalytic sites of ceria nanoshapes have strong relationship with their corresponding OVs concentrations, so they might be important in enhancing the catalytic ozonation. Therefore, Raman spectroscopy (Fig. 2B) was applied to characterize the presence of OVs. An intense band at approximately 460 cm^{-1} was corresponded to the F_{2g} mode of two oxygen atoms, whereas the weak band observed at about 597 cm^{-1} was attributed to Frenkel-type OVs [45]. The ratio of the peak areas (I_{597}/I_{460}) estimate the relative abundance of OVs in ceria [46]. According to this I_{597}/I_{460}, the concentration of OVs followed the order of R300-CeO_2 > C300-CeO_2 > O300-CeO_2 > R500-CeO_2 > NP-CeO_2. Theoretical investigations revealed that the oxygen vacancy formation energy of ceria obeys the order of (111) > (100) > (110). The concentration of OVs in CeO_2 nanorods decreased at the calcination temperature of 500 °C, suggesting that the high calcination treatment eliminated OVs which was in agreement with the XPS

To get further insight into the surface basicity of ceria nanoshapes, TPD-CO_2 was employed to measure it directly. As observed in Fig. 2C, the surfaces of CeO_2 nanoshapes were heterogeneous presenting sites of different strengths for the adsorption of CO_2. The peaks at lower temperatures ranges were assigned to weak basicity while at high temperatures were attributed to strong basicity. The higher peak area was corresponded to stronger basicity. The surface basicity followed the order of R300-CeO_2 > C300-CeO_2 > O300-CeO_2 > R500-CeO_2 > NP-CeO_2. Usually on metal oxides, two types of basic active sites such as basic OH groups as well as basic surface oxygen (Lewis base) exist. The weak and strong surface basicity are due to the difference in surface coordination unsaturation status of the cerium as well as O^{2-} and the quantity of surface defect sites. On the (111), (100) and (110) facets, the coordination number for Ce^{4+} is 7, 6, 6 respectively, while that of O^{2-} is 3, 2 and 3 respectively [47]. Moreover, due to OVs, the basicity of these nanoshapes are improved [48]. In other words, the ceria nanorods and nanocubes have relatively more defective sites than the nanooctahedra [49]. To certain extent, the stronger basic sites on nanorods and nanocubes are due to the presence of OVs. The most defective nanorods surface showed stronger basicity and the least defective ceria octahedra depicted the lowest basicity. Furthermore, surface OH groups were directly quantified by TGA (Fig. 2D), which were in accordance with TPD-CO_2. The weight losses at about 120–650 °C were

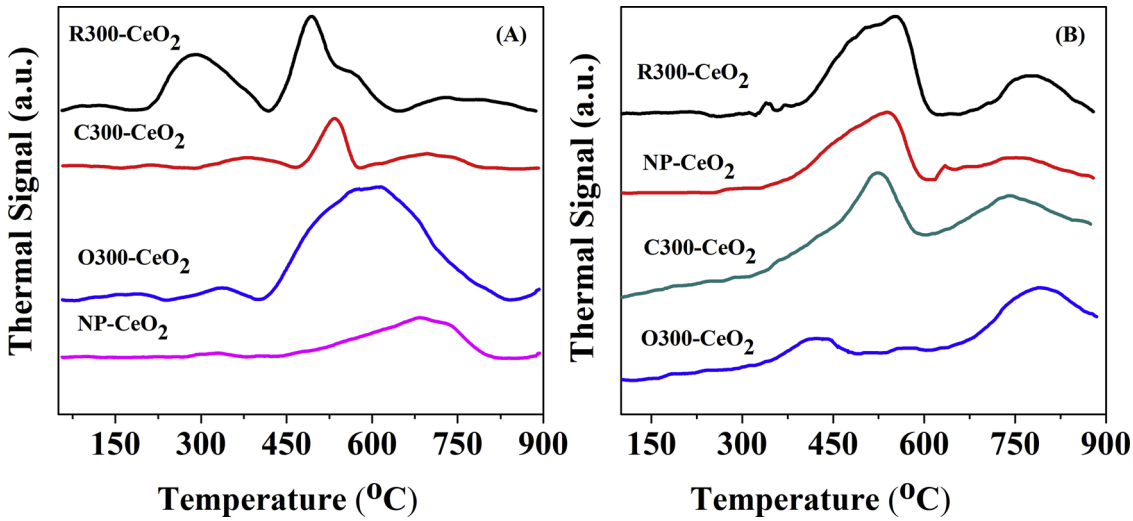

Fig. 3. (A) TPD-O_2 and (B) TPR-H_2 of ceria catalysts.

due to weakly and strongly-bonded surface OH groups [50]. The surface OH group's concentrations of R300-CeO_2, C300-CeO_2, O300-CeO_2, R500-CeO_2 and NP-CeO_2 were 4.07, 2.27, 2.10, 1.85 and 1.0% respectively. Zeta potentials of selected R300-CeO_2 were determined at different pH values to investigate the surface charge and basicity (Supporting Information, Fig S3). The pH_{PZC} value (8.72) of selected R300-CeO_2 is in agreement with its acid/base characteristics, higher value of pH_{PZC} was consistent to higher basicity.

TPD-O_2 analysis is used to quantify OVs and lattice oxygen. In the desorption profiles, peaks at lower and higher temperature ranges were observed (Fig. 3A). The O_2 desorption peaks observed at about 185–420 °C, 287–465 °C, 240–400 °C, 270–380 °C and 180–278 °C for R300-CeO_2, C300-CeO_2, O300-CeO_2, R500-CeO_2 and NP-CeO_2 were corresponded to the chemically adsorbed O_2 (ads-O_2) on OVs while the rest of wider peaks at higher temperature ranges were attributed to atomic/lattice oxygen evolved from the bulk of ceria [51]. So based on the ads-O_2 peaks area, the estimated surface concentration of OVs followed the pattern of R300-CeO_2 > C300-CeO_2 > O300-CeO_2 > NP-CeO_2.

The reduction process of surface and bulk ceria catalysts was investigated by TPR-H_2. Generally, the TPR-H_2 of ceria consists of two reduction peaks, corresponded to two-phase reduction processes: at low temperature, the reduction of the most easily reducible surface-capping Ce^{4+}/ surface oxygen species, and then the reduction of bulk ceria/bulk oxygen species at relatively higher temperature [52]. As shown in Fig. 3B, ceria catalysts depicted a low-temperature peak at about 310 °C–630 °C while a high-temperature peak at about 615 °C–885 °C. R300-CeO_2 showed the strongest reduction peak at lower temperature range while O300-CeO_2 showed a weaker peak at lower temperature and the reduction predominantly occurred at above 610 °C. The weaker peak might be related to the lowest specific surface area of O300-CeO_2 as well as due to lower content of reducible surface Ce^{4+}. Based on low temperature peak area, R300-CeO_2 depicted a potential of higher surface reducibility, so a better catalytic activity in redox reactions may be foreseen.

The N_2 sorption isotherms of catalysts depicted a type IV behavior with a distinct H1-type hysteresis, showing the mesoporous characteristics of catalysts (Supporting information, Fig. S4 A and B). The BET specific surface areas, pore diameter and pore volumes of nanorods and nanoparticles were much higher than those of nanooctahedra and nanocubes (Table 1). Furthermore, BET specific surface area of selected nanorods also decreased at calcination temperature of 500 °C due to sintering.

Table 1
Textural characteristics of all catalysts.

Catalyst	BET Surface Area (m^2g^{-1})	Pore diameter (nm)	Pore Volume ($cm^{-3}g^{-1}$)
R300-CeO_2	153.80	3.43	0.47
C300-CeO_2	47.91	2.49	0.20
O300-CeO_2	39.80	2.79	0.13
R500-CeO_2	141.20	3.46	0.56
NP-CeO_2	64.30	3.46	0.11

The oxidation states of cerium and the relative abundance/concentration (%) of surface Ce^{3+} on ceria nanoshapes were investigated by XPS analyses. The XPS spectra of R300-CeO_2 will be shown in section 4.4. The Ce 3d spectra could be split into 10 corresponding peaks by using the XPSPEAK4.1 software. Fig. 4 shows Ce 3d XPS spectra of ceria nanoshapes. The Ce 3d spectra consisted of 2 pairs of doublets as v_0, u_0 and v′, u′ attributed to the presence of Ce^{3+} and 3 pairs of doublets as v, u, v″, u″ and v‴, u‴ correspondent to the concentration of Ce^{4+}. In each doublet, v and u indicated $3d_{5/2}$ and $3d_{3/2}$ spin–orbit splits of Ce respectively. These observations showed the existence of Ce^{3+}/Ce^{4+} as redox couple on the ceria nanoshapes surfaces. Similarly the O1s XPS spectra showed two different bands at approximately 529.0 and 531.0 eV assigned to lattice oxygen (O_L) and OVs /OH groups/ adsorbed oxygen (O_A) respectively. The Ce^{3+} (%) concentration can be calculated from the ratio the peaks areas as shown in Eq. (1):

$$Ce^{3+} = \frac{A_{v0}+A_{v'}+A_{u0}+A_{u'}}{A_{v0}+A_{v'}+A_{u0}+A_{u'}+A_{v}+A_{v''}+A_{v'''}+A_{u}+A_{u''}+A_{u''}} \times 100\% \quad (1)$$

The relative concentration (%) of Ce^{3+} on the surface of R300-CeO_2, C300-CeO_2, O300-CeO_2, R500-CeO_2 were 38.30%, 34.72%, 29.25% and 27.29% respectively. Generally, the presence of relatively higher Ce^{3+} concentration indicate more OVs, observing the formation energy of oxygen vacancy with (110) < (100) < (111) trend. Similarly the O_A concentration for the above mentioned nanoshapes were 41.26%, 36.31%, 33.72% and 31.76% respectively, suggesting the same order as that of Ce^{3+}. Furthermore, for instance, calcination of nanorods at 500 °C decreased the surface concentration of Ce^{3+}. Similarly, this high calcination temperature also declined OVs due to oxidation [53].

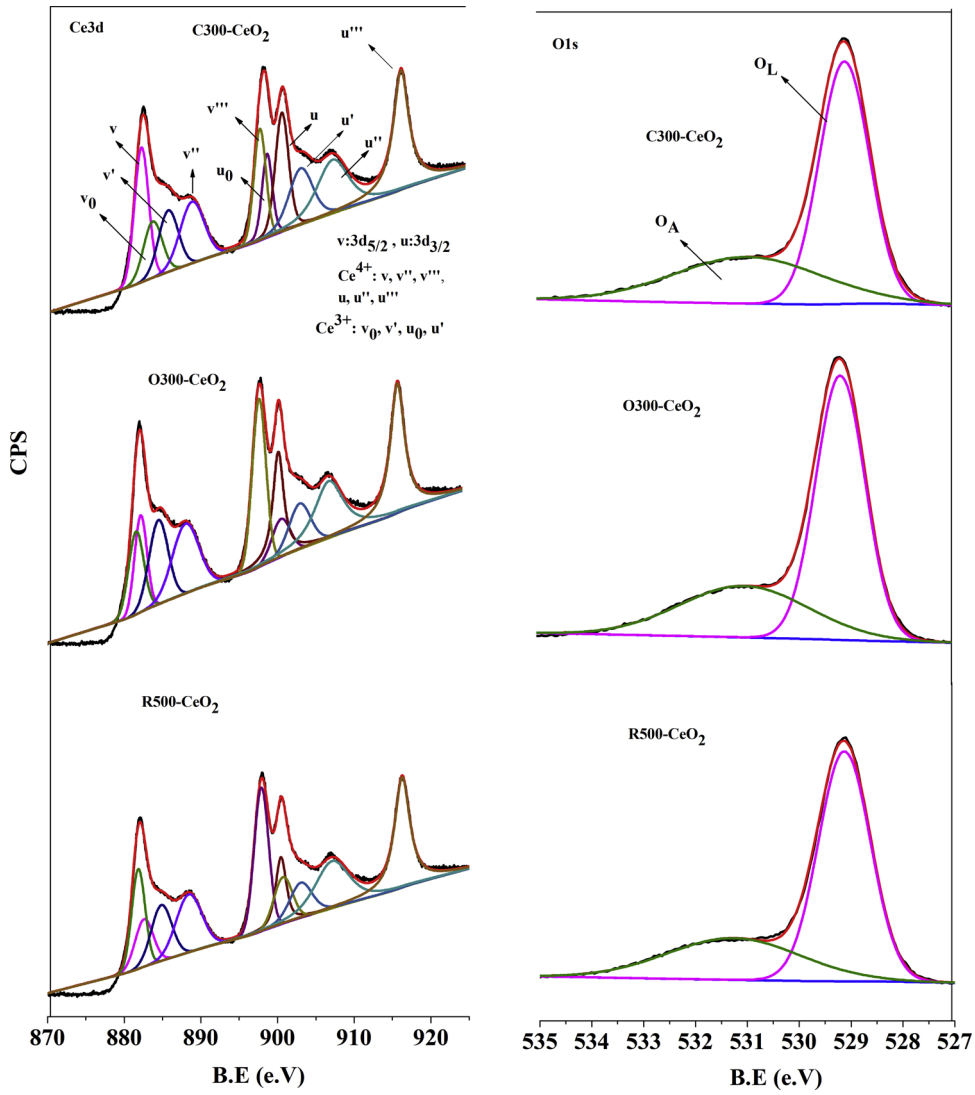

Fig. 4. XPS Spectra of Ce3d and O1s of ceria catalysts.

3.2. Comparative catalytic efficiency in different processes

Generally, sole ozonation cannot efficiently remove TOC than catalytic ozonation, so mineralization efficiency of all catalysts was investigated. Nearly 40% TOC was removed by single ozonation, while 86%, 71%, 68%, 64% and 60% TOC was removed by ozonation catalyzed by R300-CeO_2, C300-CeO_2, CeO_2-NP, O300-CeO_2 and R500-CeO_2 respectively (Fig. 5A). The adsorption capability of all catalysts surfaces was so minimal that their contribution to TOC removal could almost be neglected (data not shown for brevity). It is evidenced that the nature of exposed crystals facets altered the catalytic activity with (100) and (110) the most efficient than (111). The pattern followed by catalytic activity is in agreement with the concentrations of Ce^{3+}, surface basicity in the form of OH groups or OVs. This phenomenon indicated that the basic groups/ OVs played an important role in catalytic ozonation. The surface basicity of catalysts is imperative in improving the O_3 decomposition to ROS (reactive oxygen species) owing to electrophilic nature of O_3 [54,55]. As R300-CeO_2 showed the best catalytic activity in terms of TOC removal and ozone decomposition (section 4.2.) owing to improved surface properties, so it will be used in the onward experiments otherwise specified.

Corresponding to mineralization, in ozonation alone and ozonation catalyzed by R300-CeO_2, the pH of PNP solution declined from 5.75 to 3.30 and 5.40 respectively. This phenomenon is due to the acidic organic intermediates formation (Fig. 5B). The higher final pH value in catalytic ozonation than in sole ozonation suggested that the acidic intermediates were not accumulated but further mineralized due to the generation of ROS. As the ceria nanoshapes were synthesized in strong basic medium (NaOH solution), so before carrying out the experiments, the influence of catalysts on pH of solution was evaluated, but showed minor effect as they were heavily rinsed with ultra-pure water until neutral pH.

In ceria nanoshapes, some important surface characteristics such as surface basicity (basic OH groups and basic surface oxygen), abundance of OVs and the relative Ce^{3+} concentration are facet dependent. As already mentioned in Raman spectroscopy the relative abundance of OVs followed the order of R300-CeO_2 > C300-CeO_2 > O300-CeO_2 > R500-CeO_2 > NP-CeO_2. Similarly in XPS analysis, the surface Ce^{3+} concentration followed the same aforementioned order. Furthermore, according to TPD-CO_2 results, R300-CeO_2 showed the strongest surface basicity amongst all the ceria catalysts. The strongest surface basicity of R300-CeO_2 was due to its comparatively high defective nature in terms of OVs. TGA data also showed the highest concentration of surface OH groups for R300-CeO_2. Moreover, TPD-O_2 results showed that the R300-CeO_2 catalyst depicted the highest surface concentration of OVs. Based on aforementioned characteristics, R300-CeO_2 showed comparatively better catalytic activity as compared to other ceria catalysts.

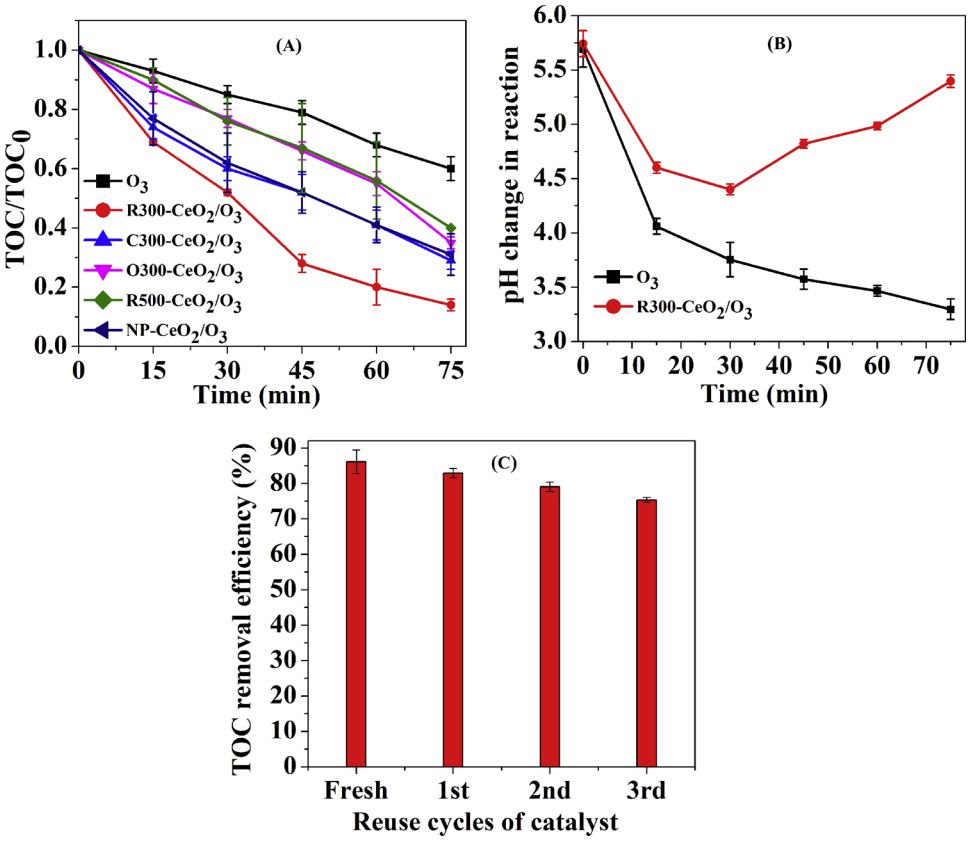

Fig. 5. (A) Comparative TOC removal in different processes, (B) pH change of solution during reaction in ozonation catalyzed by R300-CeO_2 and (C) Recycling use of R300-CeO_2. Experimental conditions: flow rate of O_3 = 1.60 mg min^{-1}, O_3 concentration in gas phase = 8.0 mg L^{-1}; volume of PNP solution = 250 mL, catalyst doze (if used) = 0.40 g L^{-1}, concentration of PNP = 25 mg L^{-1}, initial pH of solution = 5.75, temperature = 25 °C.

Previous investigators have used PNP in ozonation and catalytic ozonation. For instance, in sole ozonation and ozonation catalyzed by granular activated carbon and calcined bauxite, various organic intermediates such as hydroquinone, pyrocetechol, phenol, 4-nitrocatechol, *p*-benzoquinone, benzoquinone, formaldehyde, resorcinol and acetic anhydride were produced from PNP degradation. Some short chained organic acids such as acetic, oxalic, maleic, fumaric, muconic, formic and gyoxylic acids were also detected. The pathways of degradation were also proposed [56–58]. Moreover, a detailed discussion on the toxicity of notable byproducts can be found in the literature. Catechol could be cytotoxic, immunotoxic, and genotoxic [59–61]. Catechol caused damage to DNA as well as to protein and cell death in human [62,63]. Hydroquinone induced tremors, convulsions and acute neurobehavioral effects in animals, higher toxicity in aquatic organisms, mononuclear cell leukemia, renal cell tumors [64,65]. *p*-benzoquinone caused cell lethality and DNA damage in Chinese hamster V79 cells, and damage to lung cells [66,67]. However, in our research work, due to high mineralization efficiency (86%) of R300-CeO_2/O_3 process, most of the byproducts have been degraded into CO_2 and H_2O. So the concentration of these byproducts would be so minimum that they would not cause toxicity.

3.3. Stability of R300-CeO_2

For stability test, the used R300-CeO_2 was recycled after catalytic reaction and further washed several times with de-ionized water. TOC removal decreased from approximately 86.14% to 82.95%, 79.0% and 75.38% in the first, second and third recycling runs respectively, suggesting that the catalytic activity in the second and third cycle was approximately stable (Fig. 5C). Moreover, 3.0 μg L^{-1} cerium leaching from R300-CeO_2 was detected. To explore the role of leached cerium, homogenous catalysis with 3.0 μg L^{-1} cerium was carried out but showed negligible influence on catalytic ozonation (data not shown). The data regarding recycling and leaching experiments showed that the catalyst is stable to apply in water treatment.

4. Discussion on mechanism of catalytic ozonation

4.1. Role of surface area and surface reaction

As a matter of fact, the surface basicity of CeO_2 nanoshapes depends upon surface area and the exposed crystal facets. This phenomenon gives rise to our interest to get an insight into further exploring the influence of both exposed crystal facets and surface area on catalytic efficiency. As a matter of fact, these ceria nanoshapes have different surface area and exposed crystal facets. So it is hard to distinguish their contributions to catalytic ozonation since both surface area as well as crystal facet might be important in enhancing the catalytic activity. For this purpose, an experimental investigation was performed to exclude the influence of the surface area. For instance, different calculated doze of C300-CeO_2 but with same specific surface area was used for testing the comparative catalytic activity. The loading surface area was calculated by changing the catalyst amount. Herein, the concentration of R300-CeO_2 was fixed at 0.40 g/L. Since S_{BET} of R300-CeO_2 was 153.80 m^2/g in R300-CeO_2 /O_3 process, so the loading surface area would be 153.80 m^2/L. Therefore the concentrations of C300-CeO_2 was calculated to be nearly 1.60 g/L for keeping the same surface area loading (as that of R300-CeO_2). As shown in Fig S5 (Supporting Information), catalytic activity was still lower than that of R300-CeO_2 and approximately same as that of lower loading (0.4 g/L) of C300-CeO_2. Herein, this phenomenon depicted that different exposed crystal facets are important for enhancing catalytic ozonation rather than exposed surface area of ceria nanoshapes. This phenomenon showed that the exposed facets enhanced the catalytic activity following the order of (100 + 110) > (100) > (111). The different coordination and arrangement of Ce and O atoms significantly altered the surface reactivity

and ultimately the catalytic efficiency of ceria nanoshapes. As already mentioned in Section 3.1, due to difference in surface coordinative unsaturation of different facets, it showed different behavior in interaction with adsorbates. It is easy for reactants to react with the coordinatively unsaturated sites/lower coordination sites, which are thought to be also the active sites for enhancing catalytic activity. Furthermore, with lower coordination number, the reactivity of the reactive sites become higher [49].

OVs have rich localized electrons for the activation/dissociation of various molecules [68]. These OVs are electron donor entity which function as catalytically actives sites to dissociate ozone into ROS. So an enhanced catalytic efficiency is not solely dependent on the redox property (Ce^{3+}/Ce^{4+}) of ceria but also on the relative abundance of OVs on these ceria nanoshapes. To sum up it all, the coordination number and the amount of unsaturated coordination sites on ceria follow (1 1 1) > (1 0 0) ≈ (1 1 0) for Ce^{4+} and (1 1 1) ≈ (1 1 0) < (1 0 0) order for O^{2-} which govern the surface basic properties and hence the catalytic activity.

Ceria with different exposed crystal facets and surface coordinative unsaturation show different degree of interaction with surface adsorbates. Furthermore, the reactants can easily interact with the coordinatively unsaturated sites. So such characteristics can also alter the adsorption ability of organic intermediates produced during ozonation which are important for enhancing the efficiency of catalytic ozonation. It may give an insight to further investigate the role of surface reaction for mineralization. In case, adsorption of organic intermediates is taking place, then it maybe visualized that organic intermediates adsorbed and mineralized simultaneously on these facets by O_3/ reactive oxygen species. To get this insight, at first PNP was ozonated for 60 min, followed by purging with N_2 flow to quench/vanish the dissolved ozone. The resulted solution containing PNP degradation products was stirred with ceria nanoshapes for 75 min in the absence of ozone. Approximately 28.84% TOC was removed in adsorption by R300-CeO_2 as compared to negligible/almost no adsorption by nanocubes and nanooctahedra. This phenomenon indicated the adsorption of organic intermediates on the R300-CeO_2 and their ultimate mineralization took place or simultaneously adsorption and mineralization on the catalyst surface by O_3/reactive oxygen species took place. These differences of organic intermediates adsorption could be correspondent to the variation in surface features such as the coverage of surface OH groups. Similarly the different arrangement and coordination of Ce and O atoms on these ceria nanoshapes significantly influenced the adsorption of these organic intermediates. In ceria nanoshapes, Ce^{4+} is 6-fold coordinated on the (110) and (100) facets while 7-fold coordinated on (111) facet, due to which the Ce^{4+} sites on the surface of nanorods and nanocubes have the ability to bind/keep various adsorbates relatively more strongly than that on (111) facet. The adsorbates could easily interact with the coordinatively unsaturated sites/lower coordination sites which in turn enhanced the catalytic activity [49].

4.2. Comparison of O_3 decomposition

The decomposition of ozone into ROS on catalyst surface is important for enhancing the efficiency of catalytic ozonation. In order to explore this interaction, ozone decomposition in deionized water in the presence and absence of ceria catalysts was investigated without adding any PNP. As compared to single ozonation, ozone decomposition was more rapidly enhanced in the presence of different nanoshapes as compared to single ozonation at each instant of time (Fig. 6A), suggesting that these nanoshapes were beneficial to decompose ozone into reactive oxygen species, which is significant for improving the catalytic ozonation. R300-CeO_2 and C300-CeO_2 were the most efficient catalysts for ozone decomposition than other ceria catalysts, while the rest of catalysts showed nearly same decomposition. As a matter of fact, the cerium in these surface largely exist as Ce^{4+}, while the Ce^{3+} and the OVs are supposed to be the active sites for the decomposition of ozone [69]. As depicted by XPS measurement and Raman Spectroscopy, the active site density of R500-CeO_2 in terms of Ce^{3+} concentration, OVs, basicity and surface OH group's concentration changed due to calcination, which showed a declining impact on the O_3 decomposition. Higher Ce^{3+} concentration favored O_3 decomposition. Moreover, as compared to other nanoshapes, R300-CeO_2 with abundant OVs efficiently decomposed ozone into reactive oxygen species, suggesting that ozone decomposition could mainly occur at the sites of OVs. DFT calculation by previous investigators showed that the surface OH groups can keep the surface energy to be lower and stabilize the ceria surface by hybridization of orbital with the surface cerium and oxygen atoms; so that, in turn, the OV can be stabilized with the neighboring surface OH [70]. As the calcination at 500 °C significantly reduced the concentration of surface hydroxyl groups on R500-CeO_2, so R300-CeO_2 with relatively higher concentration of OVs efficiently decomposed ozone.

4.3. Influence of changing initial pH values on catalytic efficiency

Usually in catalytic processes, changing the initial pH of solution can alter the chemical characteristics of catalyst surface, charge on ionic organic molecules and decomposition of O_3 into active oxygen species. The pHpzc of R300-CeO_2 is 8.72, so its surface would be protonated ($CeOH^{+2}$), neutral (CeOH), or deprotonated (CeO^-) when pH value is significantly below, equal or significantly above 8.72. As shown in Fig. 6B, at the pH range of 3.0–9.0, the removal of TOC progressively enhanced, while at pH 12 (deprotonated surface), it was significantly decreased. As compared to protonated and deprotonate surfaces, TOC removal was the highest at neutral charged surface (pH 9.0 ~ pH_{pzc}) or at the natural pH (5.75) of solution, followed the order of neutral surface > protonated surface (at pH = 3.0) > deprotonated surface. This phenomenon depicted that the catalyst showed good catalytic activity at a wide pH range of 3.0-9.0. For O_3 interaction with the surface of catalyst, OH^{+2} of protonated surface has a weaker nucleophilic behavior than the oxygen of CeOH, while CeO^- surface is lack of electrophilic H to provide it for O_3. Therefore these two surfaces could minimize the interaction of ozone with surface OH which ultimately declined the catalytic activity. As in this experiment, at pH 5.75 < 8.72, the $CeOH_2^+$ surface also showed enhanced catalytic activity, attributed to resonance structures of ozone which interacted with Bronsted acid (in the form of $-OH_2^+$) through electrostatic forces and/or H-bonding for generating ROS. Furthermore, $CeOH^{+2}$ favored the organic acids adsorption but CeO^- surface could be unable to favor the adsorption of organic acidic intermediates owing to weaker electrostatic forces. At about pH 12.0 (CeO^- surface) catalytic activity decreased due to decline in the mineralization rate of organics in the solution and on R300-CeO_2 surface [2]. This phenomenon depicted that mineralization of organic intermediates took place both on the R300-CeO_2 surface as well as in the solution.

4.4. Nature of reactive oxygen species (ROS) produced and active sites

In our experimental work, catalytic ozonation was used for the mineralization of PNP, so using TBA as a $^{\cdot}OH$ scavenger can increase the TOC, therefore it is not suitable to use it. However, in water, the presence of HCO_3^- and CO_3^{2-} also behave as strong $^{\cdot}OH$ scavenger owing to higher reaction rate constants of 8.5×10^6 M^{-1} s^{-1} and 3.9×10^8 M^{-1} s^{-1} respectively with $^{\cdot}OH$ [71]. Carbonate radicals ($CO_3^{-\cdot}$) are produced due to their reaction with $^{\cdot}OH$ (Eqs. (2) and (3)).

$$HCO_3^- + {}^{\cdot}OH \rightarrow CO_3^{-\cdot} + H_2O \quad (2)$$

$$CO_3^{2-} + {}^{\cdot}OH \rightarrow CO_3^{-\cdot} + HO^- \quad (3)$$

At about neutral pH, HCO_3^- is the dominant inorganic carbon in water. Therefore for increasing its concentration, pH of PNP solution was raised to 9.0 so that it can be the main scavenger of $^{\cdot}OH$ [71].

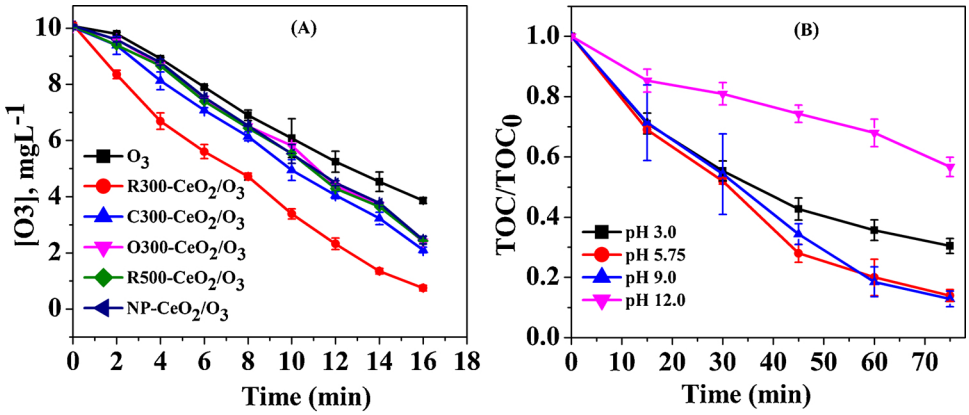

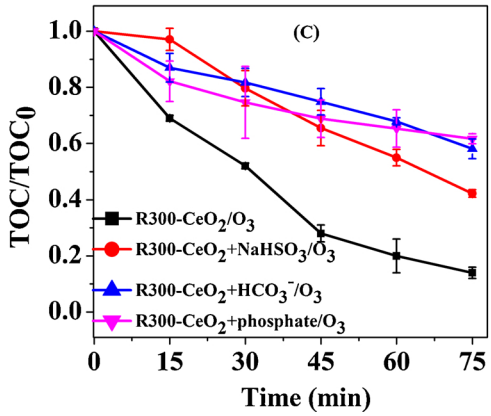

Fig. 6. (A) O_3 decomposition in the presence and absence of different ceria catalysts. Experimental conditions: aqueous ozone concentration = 10.0 mg L^{-1}; catalyst doze = 0.40 g L^{-1} temperature = 25 °C, initial pH = 5.75 (B) Influence of different initial pH values on catalytic activity. (C) Effect of ˙OH scavengers and phosphate on catalytic ozonation. Experimental conditions for Fig A, B and C are same as in Fig. 5 except different pH values in Fig. B, while pH 9 for bicarbonate experiment in Fig. C.

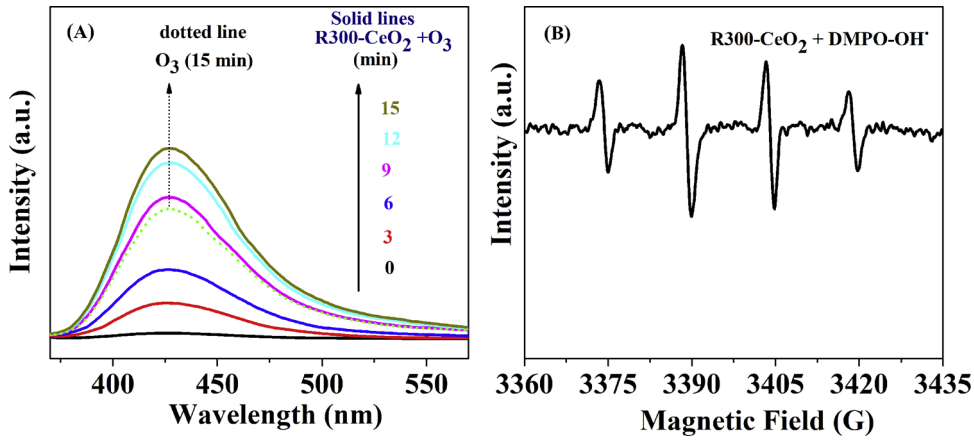

Fig. 7. (A) Florescence spectroscopy for detecting ˙OH in ozonation and ozonation catalyzed by R300-CeO_2, (B) EPR for detecting ˙OH in ozonation catalyzed by R300-CeO_2.

300 ppm HCO_3^- significantly declined the efficiency of catalytic ozonation, suggesting that HCO_3^- scavenged ˙OH (Fig. 6C). This phenomenon indicated that ˙OH were produced for efficient TOC removal. Another ˙OH scavenger, $NaHSO_3$ was also used to further get an insight into the involvement of ˙OH in enhancing the catalytic activity. As shown in Fig. 6C, 300 ppm $NaHSO_3$ significantly inhibited TOC removal, suggesting that the ˙OH were produced in catalytic ozonation. Similarly surface hydroxyl groups of catalyst can be replaced by phosphate, which can decline the binding of ozone with catalyst [1]. TOC was significantly reduced with the use of 50 mM phosphate in catalytic ozonation (Fig. 6C), suggesting that phosphate alleviated the interaction of ozone with the OH groups of the catalyst. Moreover, phosphate can also act as ˙OH scavenger (Eqs. (4), (5)).

$$^{\cdot}OH + H_2PO_4^- \rightarrow OH^- + H_2PO_4^{\cdot} \quad (4)$$

$$k_2 < 10^5\ M^{-1}\ s^{-1}$$

$$^{\cdot}OH + HPO_4^{2-} \rightarrow OH^- + H_2PO_4^- \quad (5)$$

$$k_2 < 10^7\ M^{-1}\ s^{-1}$$

Furthermore, ˙OH was detected in florescence spectroscopy by using terephthalic acid as a probe molecule. It reacts with ˙OH to produce a fluorescent 2-hydroxyterephthalic acid [72]. The concentration of this compound is directly proportional to peak intensity and so to the amount of ˙OH. Approximately at 425 nm, the peaks were intensified with the passage of time attributed to enhanced generation of ˙OH in ozonation catalyzed by R300-CeO_2 (Fig. 7A) than in sole ozonation (after 15 min) due to abundance of ˙OH.

For direct trapping of free radicals, DMPO as a spin-trapping reagent was applied in EPR to detect ˙OH as well as superoxide (˙O_2^-) while

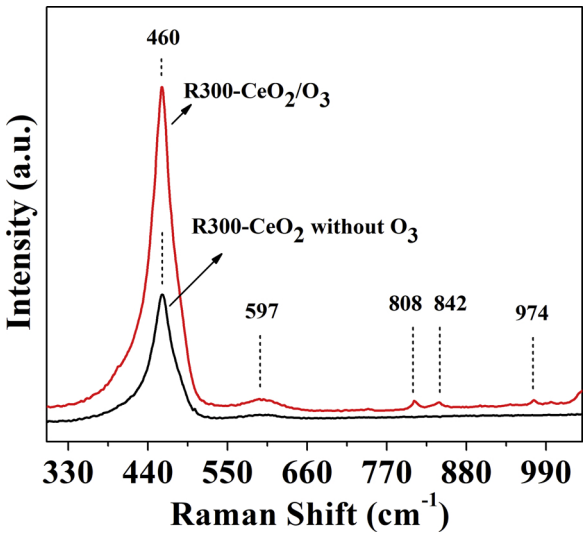

Fig. 8. Raman spectroscopy of R300-CeO_2 with and without ozone aqueous solution.

TEMP was used for probing singlet oxygen ($^1O_2$) produced during catalytic ozonation. A spectrum observed with quartet lines having characteristics 1:2:2:1 peak height ratio of the DMPO–$^{\cdot}$OH adduct is attributed to the $^{\cdot}$OH generation (Fig. 7B). For detecting $O_2^{\cdot -}$, methanol was used instead of ultrapure water as a $^{\cdot}$OH scavenger as well as to prolong the longevity of $O_2^{\cdot -}$. Furthermore, neither the peaks of the DMPO–$O_2^{\cdot -}$ adduct nor that of TEMPO adduct was observed, suggesting that $O_2^{\cdot -}$ and $^1O_2$ were not produced in catalytic ozonation (data not shown for brevity).

O_3 decomposition can also generate intermediate ROS such as surface peroxide (O_2^{2-}) and surface atomic oxygen (O^-) which can also enhance the efficiency of catalytic ozonation. Raman spectroscopy is an excellent tool to probe these species. Fig. 8 depicts the Raman spectroscopy of selected CeO_2-R300 in the absence and presence of O_3 saturated solution. The features at 597/460 cm^{-1} were ascribed to lattice OVs in ceria. Moreover, in the presence of ozone, the new peaks appeared at about 808–842 and 974 cm^{-1}, which were the representative peaks of surface peroxide (O_2^{2-}) and surface atomic oxygen (O^-) species respectively, attributed to the generation of ROS in catalytic ozonation [73]. Our results depicted that OVs and redox couple (Ce^{3+}/Ce^{4+}) on the R300-CeO_2 surface acted as the active sites. As shown in Fig. 9 (step a) O_3 could adsorb onto R300-CeO_2, it might be decomposed into surface atomic oxygen ($^*O^-$) and O_2 (Fig. 9 step b). This surface atomic oxygen would react with another O_3 molecule producing a surface peroxide species ($^*O_2^{2-}$) and O_2 as shown in Fig. 9 step c [42,73]. Ultimately these active oxygen species then decomposed the organic intermediates (Fig. 9 step d). The generation of these species on active sites other than OVs is shown in the following Eqs. (6) and (7).

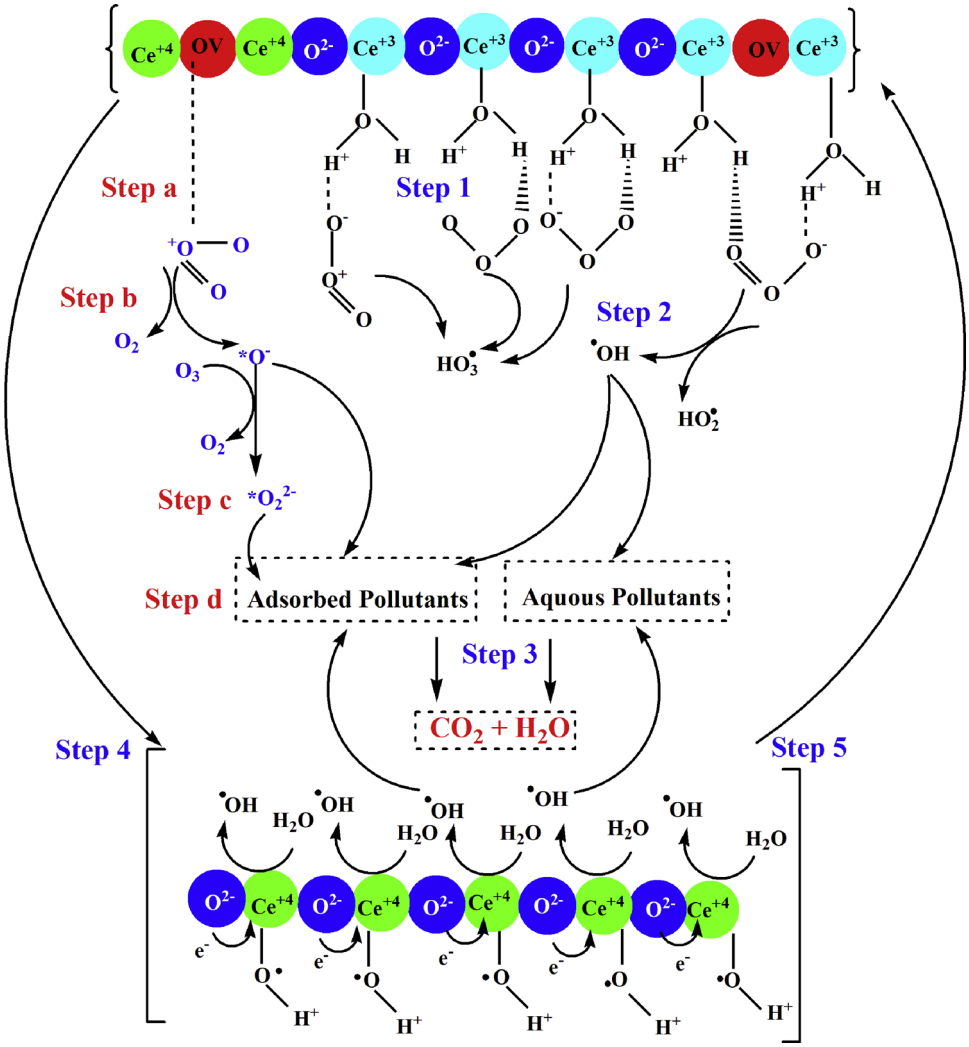

Fig. 9. Schematic representation of ozonation mechanism catalyzed by R300-CeO_2.

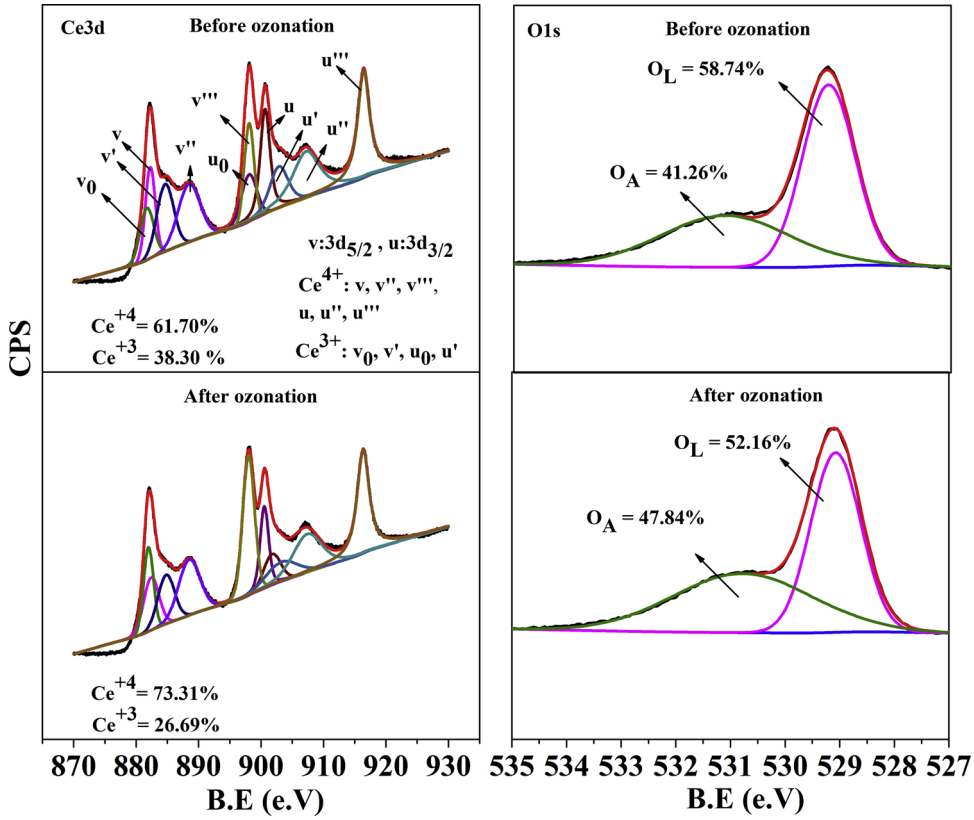

Fig. 10. XPS spectra of Ce3d and O1s before and after ozonation of R300-CeO_2.

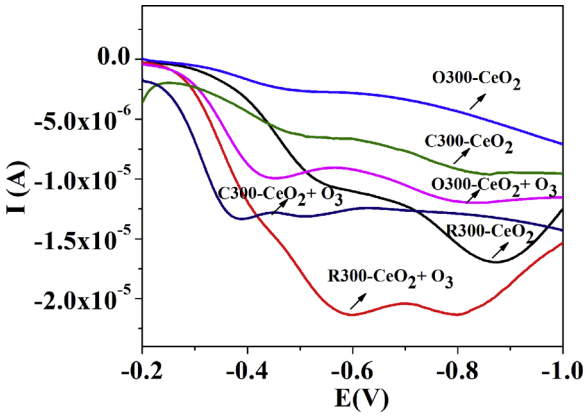

Fig. 11. LSV of nanoshapes with and without O_3 saturated solution.

Here the symbol S represents a surface active site.

$$CeO_2\text{-}S + O_3 \rightarrow CeO_2\text{-}S^*O^- + O_2 \quad (6)$$

$$CeO_2\text{-}S^*O + O_3 \rightarrow CeO_2\text{-}S^*O_2^{2-} + O_2 \quad (7)$$

XPS analyses were conducted to determine the oxidation states of surface cerium/oxygen species on the selected R300-CeO_2 before and after ozonation. The composition of Ce^{4+} increased from 61.70% to 73.31% while Ce^{+3} decreased from 38.30% to 26.69%, attributed to oxidation of Ce^{+3} to Ce^{+4} by O_3 (Fig. 10). Moreover, after ozonation, the content of lattice oxygen (O_L) decreased from 58.74% to 52.16%, while that of adsorbed oxygen (O_A) increased from 41.26% to 47.84%. This phenomenon indicated that an increase in O_A was attributed to the development of OH groups on catalyst surface. The decline in O_L concentration might be due to its utilization in reduction of Ce^{4+} to Ce^{+3}. These results depicted that O_L and surface OH groups played their role in the catalytic ozonation [74]. XPS analyses showed that the percent composition of Ce (Ce^{+3}/ Ce^{4+}) as well as oxygen changed. Hence, it is depicted that the surface R300-CeO_2 provided the active sites to ozone adsorption and activation. Ce acted as the catalytically active site to transfer electron to ozone. As shown in Fig. 9; step 1, ozone was bonded to the surface of R300-CeO_2 ($CeOH_2^+$) by electrostatic forces/H bonding, which ultimately facilitated the transformation of electron. In Fig. 9; step 2, the O—O and H—O were weakened to be decomposed into $HO_2^{\cdot}$, $HO_3^{\cdot}$ and $^{\cdot}OH$ species on the R300-CeO_2 surface. In Fig. 9; step 3, then further reactions between O_3 and $HO_2^{\cdot}$ on the R300-CeO_2 surface and in the aqueous bulk generated $^{\cdot}OH$ to mineralize PNP. For completing the redox couple and maintaining an electrostatic charge balance, the O_L would reduce Ce^{4+} to Ce^{3+} as shown in Fig. 9; step 4. This phenomenon would create surface OVs, which would ultimately increase the oxygen surface adsorption capability of the R300-CeO_2. Afterwards, the oxygen-deficiency on the R300-CeO_2 surface was compensated by O_3. In these processes, a redox cycle was followed the sequence of $Ce^{3+} \rightarrow Ce^{4+} \rightarrow Ce^{3+}$ as shown in Fig. 9; step 5. It is concluded that during this whole oxidation process, the electrons transfer from the surface of Ce^{3+} to O_3 induced the decomposition of O_3 to ROS and the O_L reduced the surface Ce^{4+} to Ce^{3+}. Hence a redox couple/electrostatic balance between Ce^{3+}/ Ce^{4+} and O^{2-}/O_2 were involved in enhancing the catalytic activity. In light of our experimental results and literature reviews [75–77] the following reactions are proposed.

$$\equiv Ce^{3+} - OH_2^+ + O_3 \rightarrow \equiv Ce^{3+} - OH_2^+ - O_3 \quad (8)$$

$$\equiv Ce^{3+} - 2\,OH_2^+ - 4\,O_3 \rightarrow \equiv Ce^{4+} + 2O^{2-} + 4HO_3^{\cdot} \quad (9)$$

$$HO_3^{\cdot} + HO_3^{\cdot} \rightarrow 2^{\cdot}OH + 2O_2 \quad (10)$$

$$2O^{-2} + H^+ \rightarrow HO_2^{\cdot} \quad (11)$$

$$HO_2^{\cdot} + O_3 \rightarrow {}^{\cdot}OH + 2O_2 \quad (12)$$

$$2O^{2-} + \equiv Ce^{4+} \rightarrow \equiv Ce^{3+} + O_2 \quad (13)$$

$$2O_3 + 4e^- \rightarrow 2O^{2-} + 2O_2 \quad (14)$$

As depicted by XPS, the redox couple (Ce^{3+}/Ce^{4+}) is important for enhancing the catalytic efficiency. For further getting an insight into this process, linear sweep voltammetry (LSV) of CeO_2 nanoshapes was performed in 0.1 M Na_2SO_4 with and without O_3. Results in Fig. 11 showed that the current signal in R300-CeO_2 was strongest, following the trend of R300-CeO_2 < C300-CeO_2 < O300-CeO_2. An obvious current on these nanoshapes suggested the presence of surface charge. Moreover, in O_3 saturated solution, an improvement in the peaks of reduction current occurred, attributed to the reduction process on the surface of ceria owing to the decomposition of ozone [78]. Furthermore, with ozonation, an increase in the reduction current on all nanoshapes followed a similar tendency as without O_3. The strongest current signal on the R300-CeO_2 electrode than the other nanoshapes suggested its high electron transfer ability to reduce ozone for the generation of reactive oxygen species.

5. Conclusion

Ceria nanorods, nanocubes and nano-octahedra with different exposed facets (110) + (100), (100) and (111) respectively) were used in ozonation of p-nitrophenol. Raman spectroscopy, TPD-CO_2 and TGA for the concentration of oxygen vacancies (OVs), surface basicity and surface OH groups respectively decreased in the order of R300-CeO_2 > C300-CeO_2 > O300-CeO_2 > R500-CeO_2 > NP-CeO_2. XPS showed that the concentration (%) of Ce^{3+} followed the order of R300-CeO_2 > C300-CeO_2 > O300-CeO_2 > R500-CeO_2. Mineralization decreased as R300-CeO_2 > C300-CeO_2 > CeO_2-NP > O300-CeO_2 > R500-CeO_2 > O_3 which is in agreement with the concentrations of surface basic sites, OVs, Ce^{3+} and OH groups. The selected R300-CeO_2 was stable too. R300-CeO_2 and C300-CeO_2 were the most efficient for O_3 decomposition than others. $^{\cdot}OH$, O_2^{2-} and O^- were the dominant ROS produced for enhancing the catalytic ozonation.

Acknowledgements

This work was supported by National Natural Science Foundation of China (No. 21590813), Program for Changjiang Scholars and Innovative Research Team in University (IRT_13R05), and the Program of Introducing Talents of Discipline to Universities (B13012).

Appendix A. Supplementary data

Supplementary material related to this article can be found, in the online version, at doi:https://doi.org/10.1016/j.apcatb.2019.02.010.

References

[1] S. Afzal, X. Quan, J. Zhang, Appl. Catal. B 206 (2017) 692–703.
[2] J. Bing, C. Hu, Y. Nie, M. Yang, J. Qu, Environ. Sci. Technol. 49 (2015) 1690.
[3] F. Zhang, K. Wu, H. Zhou, Y. Hu, H. Wu, C. Wei, J. Environ. Manage. 224 (2018) 376–386.
[4] Y. Wang, Y. Xie, H. Sun, J. Xiao, H. Cao, S. Wang, Catal. Sci. Technol. 6 (2016) 2918–2929.
[5] D. Wang, H. Xu, J. Ma, X. Lu, J. Qi, S. Song, Chem. Eng. J. 354 (2018) 113–125.
[6] D. Quiñones, A. Rey, P.M. Álvarez, F. Beltrán, G.L. Puma, Appl. Catal. B: Environ. 178 (2015) 74–81.
[7] L. Zhao, J. Ma, Z.-z. Sun, X.-d. Zhai, J. Hazard. Mater. 161 (2009) 988–994.
[8] C. Chen, X. Yan, B.A. Yoza, T. Zhou, Y. Li, Y. Zhan, Q. Wang, Q.X. Li, Sci. Total Environ. 612 (2018) 1424–1432.
[9] L. Yuan, J. Shen, P. Yan, J. Zhang, Z. Wang, S. Zhao, Z. Chen, J. Hazard. Mater. 365 (2019) 744–750.
[10] F. Boudissa, D. Mirilà, V.-A. Arus, T. Terkmani, S. Semaan, M. Proulx, I.-D. Nistor, R. Roy, A. Azzouz, J. Hazard. Mater. 364 (2019) 356–366.
[11] S. Larouk, R. Ouargli, D. Shahidi, L. Olhund, T.C. Shiao, N. Chergui, T. Sehili, R. Roy, A. Azzouz, Chemosphere 168 (2017) 1648–1657.
[12] F. Qi, W. Chu, B. Xu, Chem. Eng. J. 262 (2015) 552–562.
[13] S. Li, Y. Tang, W. Chen, Z. Hu, X. Li, L. Li, J. Colloid Interface Sci. 504 (2017) 238–246.
[14] B. Xu, F. Qi, J. Zhang, H. Li, D. Sun, D. Robert, Z. Chen, Chem. Eng. J. 284 (2016) 942–952.
[15] Y. Huang, C. Cui, D. Zhang, L. Li, D. Pan, Chemosphere 119 (2015) 295–301.
[16] Y. Liu, D. Wu, S. Peng, Y. Feng, Z. Liu, Sep. Purif. Technol. 209 (2019) 588–597.
[17] F. Zhang, C. Wei, K. Wu, H. Zhou, Y. Hu, S. Preis, Appl. Catal. A: Gen. 547 (2017) 60–68.
[18] S. Psaltou, S. Stylianou, M. Mitrakas, A. Zouboulis, Separations 5 (2018) 42.
[19] S. Afzal, X. Quan, S. Chen, J. Wang, D. Muhammad, J. Hazard. Mater. 318 (2016) 308–318.
[20] Y. Wang, Y. Xie, H. Sun, J. Xiao, H. Cao, S. Wang, ACS Appl. Mater. Interfaces 8 (2016) 9710.
[21] M. Piumetti, S. Bensaid, N. Russo, D. Fino, Appl. Catal. B Environ. 165 (2015) 742–751.
[22] M. Zheng, S. Wang, M. Li, C. Xia, J. Power Sources 345 (2017) 165–175.
[23] N. Izu, T. Itoh, W. Shin, I. Matsubara, N. Murayama, Sens. Actuators B Chem. 123 (2007) 407–412.
[24] A.K.P. Mann, Z. Wu, F.C. Calaza, S.H. Overbury, ACS Catal. 4 (2014) 2437–2448.
[25] C.A. Orge, J.J.M. Órfão, M.F.R. Pereira, A.M.D.D. Farias, R.C.R. Neto, M.A. Fraga, Appl. Catal. B Environ. 103 (2011) 190–199.
[26] C.A. Orge, J.J.M. Órfão, M.F.R. Pereira, A.M.D.D. Farias, M.A. Fraga, Chem. Eng. J. 200–202 (2012) 499–505.
[27] W. Li, Z. Qiang, T. Zhang, X. Bao, X. Zhao, J. Mol. Catal. A Chem. 348 (2011) 70–76.
[28] J. Bing, X. Wang, B. Lan, G. Liao, Q. Zhang, L. Li, Separation Purif. Technol. 118 (2013) 479–486.
[29] C. Sun, H. Li, L. Chen, Energy Environ. Sci. 5 (2012) 8475–8505.
[30] K. Zhou, X. Wang, X. Sun, Q. Peng, Y. Li, J. Catal. 229 (2005) 206–212.
[31] E. Aneggi, D. Wiater, C.D. Leitenburg, J. Llorca, A. Trovarelli, ACS Catal. 4 (2014) 172–181.
[32] K. Zhou, W. Xun, X. Sun, Q. Peng, Y. Li, J. Catal. 229 (2005) 206–212.
[33] Tana, M. Zhang, J. Li, H. Li, Y. Li, W. Shen, Catal. Today 148 (2009) 179–183.
[34] M. Baudin, M. Wójcik, K. Hermansson, Surf. Sci. 468 (2000) 51–61.
[35] H.X. Mai, L.D. Sun, Y.W. Zhang, R. Si, W. Feng, H.P. Zhang, H.C. Liu, C.H. Yan, J. Phys. Chem. 109 (2005) 24380–24385.
[36] I. Florea, C. Feralmartin, J. Majimel, D. Ihiawakrim, C. Hirlimann, O. Ersen, Cryst. Growth Des. 13 (2013) 1110–1121.
[37] L. Vivier, D. Duprez, Chemsuschem 3 (2010) 654.
[38] T.X.T. Sayle, S.C. Parker, D.C. Sayle, Phys. Chem. Chem. Phys. Pccp 7 (2005) 2936–2941.
[39] M. Li, Z. Wu, S.H. Overbury, J. Catal. 306 (2013) 164–176.
[40] X.P. Wu, X.Q. Gong, Phys. Rev. Lett. 116 (2016) 086102.
[41] Z. Wu, A.K.P. Mann, M. Li, S.H. Overbury, J. Phys. Chem. C 119 (2015) 7340–7350.
[42] T. Zhang, W. Li, J.P. Croué, Environ. Sci. Technol. 45 (2011) 9339–9346.
[43] H. Bader, J. Hoigné, Water Res. 15 (1981) 449–456.
[44] Y. Cui, W.-L. Dai, Catal. Sci. Technol. 6 (2016) 7752–7762.
[45] Y. Wang, F. Wang, Q. Song, Q. Xin, S. Xu, J. Xu, J. Am. Chem. Soc. 135 (2013) 1506.
[46] L. Li, F. Chen, J.Q. Lu, M.F. Luo, J. Phys. Chem. A 115 (2011) 7972.
[47] Z. Wu, M. Li, D.R. Mullins, S.H. Overbury, ACS Catal. 2 (2012) 2224–2234.
[48] H. Metiu, S. Chrétien, Z. Hu, B. Li, X.Y. Sun, J. Phys. Chem. C (2012) 10439–10450.
[49] Z. Wu, M. Li, J. Howe, S.H. Overbury, Langmuir ACS J. Surf. Colloids 26 (2010) 16595–16606.
[50] R. Mueller, H.K. Kammler, A. Karsten Wegner, S.E. Pratsinis, Langmuir 19 (2003) 160–165.
[51] M.J. Manto, P. Xie, C. Wang, ACS Catal. 7 (2017) 1931–1938.
[52] M. Zabilskiy, P. Djinović, E. Tchernychova, O.P. Tkachenko, L.M. Kustov, A. Pintar, ACS Catal. 5 (2015) 5357–5365.
[53] C. Zang, X. Zhang, S. Hu, F. Chen, Appl. Catal. B Environ. 216 (2017) 106–113.
[54] J. Rivera-Utrilla, M. Sánchez-Polo, Langmuir ACS J. Surf. Colloids 20 (2004) 9217–9222.
[55] J. Chen, S. Tian, J. Lu, Y. Xiong, Appl. Catal. A Gen. 506 (2015) 118–125.
[56] L. Gu, X. Zhang, L. Lei, Ind. Eng. Chem. Res. 47 (2008) 6809–6815.
[57] C. Chen, H. Chen, J. Yu, C. Han, G. Yan, S. Guo, Clean–Soil, Air, Water 43 (2015) 1010–1017.
[58] S. Shanthi, M. Yenkie, J. Pollut. Eff. Control. (2016) 1–4.
[59] G. Barreto, D. Madureira, F. Capani, L. Aon-Bertolino, E. Saraceno, L.D. Alvarez-Giraldez, Environ. Mol. Mutagen. 50 (2009) 771–780.
[60] M. Valko, M. Izakovic, M. Mazur, C.J. Rhodes, J. Telser, Mol. Cell. Biochem. 266 (2004) 37–56.
[61] N. Schweigert, R.W. Hunziker, B.I. Escher, R.I. Eggen, Environ. Toxicol. Chem. 20 (2001) 239–247.
[62] N. Schweigert, A.J. Zehnder, R.I. Eggen, Environ. Microbiol. 3 (2001) 81–91.
[63] D. De Oliveira, B. Pitanga, M. Grangeiro, R. Lima, Md.F.D. Costa, S.L. Costa, J. Clarêncio, Rd.S. El-Bachá, Hum. Exp. Toxicol. 29 (2010) 199–212.
[64] D.C. Topping, L.G. Bernard, J.L. O'Donoghue, J.C. English, Food Chem. Toxicol. 45 (2007) 70–78.
[65] H. Bährs, A. Putschew, C.E. Steinberg, Environ. Sci. Pollut. Res. 20 (2013) 146–154.
[66] F. Yang, J.-H. Zhou, J. Toxicol. Environ. Health Part A 73 (2010) 483–489.
[67] A. Das, S. Chakrabarty, D. Choudhury, G. Chakrabarti, Chem. Res. Toxicol. 23 (2010) 1054–1066.
[68] J. Lee, C.S. Dan, X. Deng, J. Am. Chem. Soc. 133 (2011) 10066–10069.
[69] E.G. Heckert, S. Seal, W.T. Self, Environ. Sci. Technol. 42 (2008) 5014–5019.
[70] X.P. Wu, X.Q. Gong, Phys. Rev. Lett. 116 (2016) 086102.
[71] J. Ma, N.J.D. Graham, Water Res. 34 (2000) 3822–3828.
[72] K.-i. Ishibashi, A. Fujishima, T. Watanabe, K. Hashimoto, J. Photochem. Photobiol. A: Chem. 134 (2000) 139–142.
[73] R. Radhakrishnan, S.T. Oyama, J. Catal. 199 (2001) 282–290.
[74] H. Zhao, Y. Dong, P. Jiang, G. Wang, J. Zhang, K. Li, C. Feng, New J. Chem. 38 (2014) 1743–1750.
[75] L. Zhao, Z. Sun, J. Ma, H. Liu, J. Mol. Catal. A: Chem. 322 (2010) 26–32.
[76] L. Zhao, J. Ma, Z. Sun, H. Liu, Appl. Catal. B: Environ. 89 (2009) 326–334.
[77] J. Bing, C. Hu, Y. Nie, M. Yang, J. Qu, Environ. Sci. Technol. 49 (2015) 1690–1697.
[78] F. Nawaz, Y. Xie, J. Xiao, H. Cao, Z.A. Ghazi, Z. Guo, Y. Chen, Catal. Sci. Technol. 6 (2016) 7875–7884.